Article

Synthetic reflection self-injection-locked microcombs

Alexander E. Ulanov ®[1], Thibault Wildi ®[1], Nikolay G. Pavlov ®[2], John D. Jost[2], Maxim Karpov[2] & Tobias Herr ®[1,3] ✉

Laser-driven microresonators have enabled chip-integrated light sources with unique properties, including the self-organized formation of ultrashort soliton pulses and frequency combs (microcombs). While poised to impact major photonic applications such as spectroscopy, sensing and optical data processing, microcombs still necessitate complex scientific equipment to achieve and maintain suitable single-pulse operation. Here to address this challenge, we demonstrate microresonators with programmable synthetic reflection providing tailored injection feedback to the driving laser. Synthetic reflection achieves independence from random sample scattering properties and, when designed appropriately, enables deterministic access to self-injection-locked microcombs operating exclusively in the single-soliton regime. These results provide a route to easily operable microcombs at scale for portable sensors, autonomous navigation or extreme-bandwidth data processing. The novel concept of synthetic reflection may also be generalized to other integrated photonic systems.

Laser-driven microresonators provide access to non-linear optical phenomena, already with low-power continuous-wave excitation[1]. Leveraging efficient non-linear frequency conversion, they have enabled novel sources of coherent laser radiation across a broad spectral span[2,3]. Soliton microcombs[4–6] are an important representative of such sources, providing frequency comb spectra of mutually coherent laser lines, based on self-organized dissipative Kerr solitons (DKSs) in resonators with anomalous group velocity dispersion[7]. Such DKS microcombs can be integrated on photonic chips[8,9] and have demonstrated their disruptive potential in many emerging and ground-breaking applications, for example high-throughput optical data transmission[10] reaching petabit-per-second data rates[11], ultrafast laser ranging[12,13], precision astronomy in support of exo-planet searches[14,15], high-acquisition-rate dual-comb spectroscopy[16], ultra-low-noise microwave photonics[17,18], photonic computing and all-optical neural networks[19–21].

To leverage microcomb technology in out-of-laboratory applications, it is critical to reliably access the DKS regime and ideally single-DKS operation[4,22–25], ensuring well-defined temporal and spectral characteristics. A critical challenge for microcombs arises from the need to stabilize the detuning $\Delta\omega_0 = \omega_0 - \omega_p$ of the pump laser ω_p with respect to the pumped resonance ω_0. While this is common to all resonant approaches, it is particularly challenging during DKS initiation, when thermo-optic effects can cause a rapid (on the order of microseconds) change in resonance frequency[4]. To overcome this challenge, a number of methods have been developed, involving rapid laser actuation[4,8], auxiliary lasers[26] and/or auxiliary resonances[27,28], laser modulation[29], additional non-linearities[25,30,31] or pulsed driving[24]. These methods are successfully used in research.

An attractive approach that can stabilize the laser detuning for DKS operation is self-injection locking (SIL). It relies on a feedback wave created through backscattering in the microresonator that effectively locks the laser frequency to the microresonator resonance[32–35]. SIL has been utilized for DKS generation in bulk whispering-gallery-mode resonators[17,36] as well as in highly integrated photonic chip-based systems[37–41]. In these SIL-based DKS sources, the feedback wave is based on Rayleigh backscattering from random fabrication imperfections or material defects in the microresonator[42]. However, critically relying on random imperfections is incompatible with scaling of microcomb technology into large volume applications. It is also at odds with the

[1]Deutsches Elektronen-Synchrotron DESY, Hamburg, Germany. [2]Enlightra Sarl, Renens, Switzerland. [3]Physics Department, Universität Hamburg UHH, Hamburg, Germany. ✉e-mail: tobias.herr@desy.de
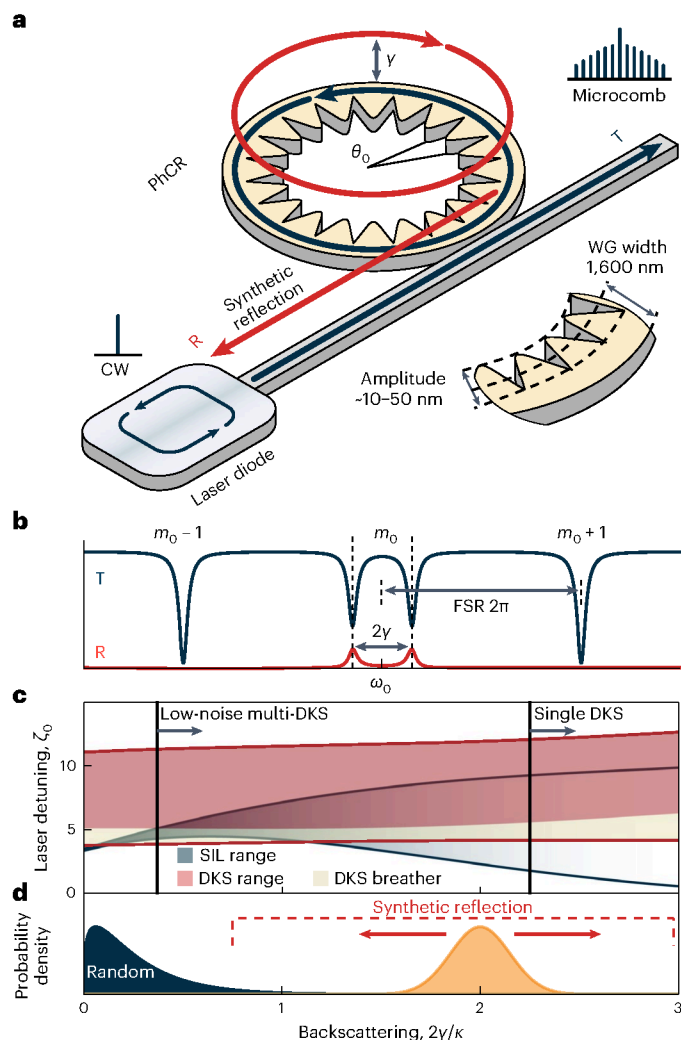
Fig. 1 | Self-injection locking with synthetic reflection. a, An integrated PhCR with a periodic corrugation (with an angular period θ_0), which induces coupling at a rate γ between forwards- and backwards-propagating waves for a mode $m_0 = \pi/\theta_0$. In addition to a transmission signal (T), this leads to a well-defined synthetic resonant reflection (R), which can be programmed for self-injection locking with a laser diode driving the system. The magnified view indicates the typical dimensions. CW, continuous wave. WG, waveguide. **b**, Indicative transmission and reflection spectra for the resonance with mode number m_0 and two adjacent resonances $m_{0\pm1}$, separated by ± 1 FSR. For $\gamma \neq 0$, mode number m_0 exhibits a split line shape (with a frequency splitting of 2γ) and shows non-zero resonant reflection. **c**, A comparison of the (non-linear) SIL and DKS existence ranges (see the main text) in units of the normalized detuning ζ_0 (Methods) as a function of the backscattering for a critically coupled microresonator with a total line width of $\kappa/2\pi = 120$ MHz and dispersion of $D_2/2\pi = 8$ MHz, driven with a normalized pump power of $f^2 = 9$. **d**, An illustration of the probability of finding a certain strength of backscattering in a conventional microresonator (blue) or in a PhCR with synthetic reflection (orange). The PhCR with synthetic reflection allows for much larger and tailored backscattering by design.

intense efforts towards reducing backscattering through improved fabrication processes.

In this Article, we introduce synthetic reflection as a novel method for self-injection locked microcombs. In contrast to previous demonstrations, this method is independent of random backscattering and permits the generation of tailored back-reflection spectrum without disturbing the dispersion profile or noticeably decreasing the quality factor Q. This is achieved deliberately in photonic crystal ring resonators (PhCR) (Fig. 1a)[43], which have recently received growing attention in integrated non-linear photonics[44–48]. We show that

synthetically created back-reflection can provide robust access to DKS states by increasing the overlap between laser detunings where DKS can exist and those detunings that can be accessed via SIL. In addition, we show that robust access to SIL-based DKS can be combined with recent results of spontaneous single-DKS generation in (not self-injection-locked) PhCRs, avoiding non-solitonic states[44]. This offers a low-complexity alternative to the method previously demonstrated in self-injection-locked systems, which required careful laser tuning to convert a multi-DKS state into a single-DKS state[40]. In combination, our results provide a route to easily operable microcombs for out-of-laboratory applications.

Results

To gain independence from random imperfections, we use PhCRs that enable synthetic reflection by design. The reflection is controlled by periodic nano-patterned corrugations of the ring resonators' inner walls. The angular corrugation period is $\theta_0 = 2\pi/(2m_0)$, where m_0 is the angular (azimuthal) mode number, for which a deliberate coupling between forwards- and backwards-propagating waves with a coupling rate γ is induced (Fig. 1a). Besides inducing the desired synthetic reflection, the coupling leads to mode hybridization, resulting in a split resonance line shape (with a frequency splitting of 2γ) in both transmission and reflection (Fig. 1b). Here, we only consider the lower-frequency hybrid mode for pumping, as it corresponds to strong (spectrally local) anomalous dispersion, which prevents high-noise comb states[49]. To choose γ, we balance multiple criteria, as detailed below.

First, a strong reflection can considerably extend the range of normalized detunings $\zeta_0 = 2\Delta\omega_0/\kappa$ (where κ is the microresonator line width) accessible via SIL (the SIL range) in a non-linear microresonator. This is crucial as it permits robust access to detunings where DKS can exist (the DKS existence range). This is exemplified in Fig. 1c, where the SIL range according to the theory by Voloshin et al.[40] is shown along with the numerically computed DKS and breathing DKS existence ranges (obtained through integration of the coupled mode equations; Methods). Note that, in a resonator with a shifted pump mode[50], the existence range of DKS deviates strongly from that known from resonators without a shifted pump mode[51] and can currently only be obtained numerically (Fig. 1c). In conventional resonators, the normalized forwards–backwards coupling is usually small ($2\gamma/\kappa < 1$; Fig. 1d) and the intersection between the SIL and DKS ranges does not exist or is limited. Synthetic reflection can reliably provide access to larger backscattering.

Second, while advantageous for an extended SIL range, stronger forwards–backwards coupling γ will also result in an increased threshold at which modulation instability (MI) occurs. Without MI, DKS cannot form inside the resonator (without external stimuli such as triggering pulses[7]). The threshold power is different from that in a conventional ring resonator[52], and its derivation critically requires consideration of the backwards wave. For strong forwards–backwards coupling ($2\gamma/\kappa > 1$) and under the assumption of pumping only the low-frequency hybrid mode, the following approximation is derived (equation (38) in Supplementary Information) for the threshold pump power

$$f_{th}^2 = 4\frac{\gamma}{\kappa} + \frac{\kappa}{\gamma},\tag{1}$$

which is normalized as detailed in Methods. The value of f_{th}^2 must not exceed the available pump power f^2. If the MI threshold is reached at a detuning within the DKS existence range, then the MI state is only transient and DKS can form spontaneously, as recently observed in PhCRs[44] and over-moded resonators[53] owing to the DKS attractor[4,54,55].

Third, by controlling the MI state that precedes the DKS, the deterministic creation of a single-DKS state can be achieved. This is the case when the first MI side-bands are separated from the pump laser by one
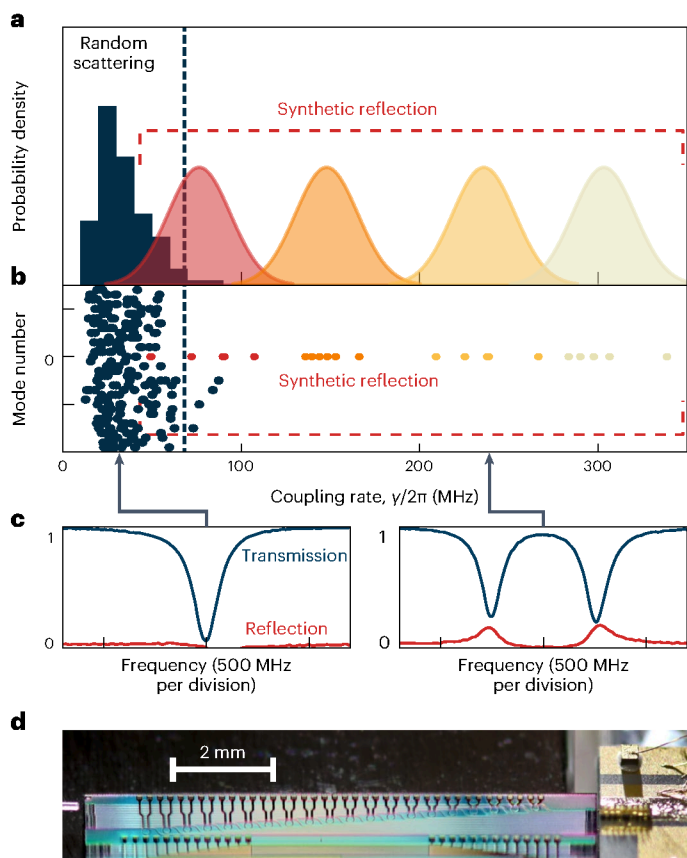
Fig. 2 | Resonator characterization. a, Distributions of the measured forwards–backwards coupling rate $\gamma/(2\pi)$ in resonances with random backscattering unaffected by synthetic reflection (blue histogram) and deliberately affected by the corrugation with four select corrugation amplitudes (red-, orange-, yellow- and beige-shaded indicative Gaussian distributions). **b**, A scatter plot of coupling rate versus mode number of the data underlying **a**. Synthetic reflection impacts only the pumped mode with relative mode number $\mu = 0$. **c**, Non-zero forwards–backwards coupling manifests as a splitting of the transmission (blue) and reflection line shapes. Left: for $\gamma < \kappa$, the splitting is unresolved; right: for $\gamma > \kappa$, the splitting is apparent. **d**, The experimental system, showing the semiconductor laser diode (right) butt-coupled to the photonic chip with the PhCRs (middle). Transmitted light is out-coupled using an optical fibre (left).

to provide anomalous dispersion as required for DKS formation. We characterized the fabricated resonators by recording their transmission spectrum in frequency comb-calibrated laser scans[56], permitting us to retrieve the coupling rates γ and the resonance widths κ via line shape fitting over a broad spectral bandwidth. Figure 2a shows the retrieved distributions of the coupling rate γ of multiple PhCRs with different corrugation amplitudes. The blue histogram reports the distribution of $\frac{\gamma}{2\pi}$ for the resonances that are not affected by the corrugation (that is, away from the pumped mode), and the red, orange, yellow and beige shadings represent the distributions of the deliberately split resonances for PhCR designs with different corrugation amplitudes (small to large, six samples for each amplitude). The underlying data are shown in Fig. 2b as a scatter plot. Although the random imperfection-based forwards–backwards coupling rate $\frac{\gamma}{2\pi}$ can in rare cases reach high values (here up to ~100 MHz, corresponding to $2\gamma/\kappa \approx 2$), the most probable value is low (here ~25 MHz, corresponding to $2\gamma/\kappa \approx 0.5$). In contrast, PhCRs enable control over the backscattering rate by design and, as shown by the experimental data in Fig. 2, provide robust access to back-reflections that are difficult or impossible to access through random imperfections. Importantly, only a single pre-defined resonance to which the PhCR's corrugation is matched exhibits large forwards–backwards coupling, while all other modes remain unaffected. This is evidenced by the data in Fig. 2b and further illustrated in Supplementary Fig. 3a. Established concepts of waveguide dispersion engineering to create dispersive waves or broadband spectra remain unaffected. No noticeable degradation of the Q factor is observed up to $\gamma/2\pi \lesssim 5$ GHz (approximately 100 times larger than what is used here), corresponding to a critically coupled line width of $\frac{\kappa}{2\pi} \approx 110$ MHz (Supplementary Fig. 3). Considering alternative resonator radii, we note that γ is mostly defined by the corrugation amplitude and only weakly dependent on the resonator's radius. A tighter radius implies a weaker effect of the corrugation owing to the shift of the mode field towards the outer rim of the resonator.

For the experiments, a semiconductor distributed feedback laser diode (DFB) was butt-coupled (without optical isolation) to the photonic chip (Fig. 2d), permitting an estimated on-chip pump power of $P = 21$ mW, corresponding to $f^2 \approx 7.3$. From equations (1) and (2), we obtain an ideal backscattering range of $2\gamma/\kappa \in (1.83, 3.35)$, ensuring deterministic and exclusive generation of a single DKS. On the basis of these considerations, we choose a PhCR with a normalized synthetic backscattering for the pump mode at 1,557 nm of $2\gamma/\kappa \approx 2.67$ ($\frac{\gamma}{2\pi} \approx 145$ MHz). This PhCR is critically coupled and exhibits anomalous group velocity dispersion ($D_2 \approx 9$ MHz; see Methods for a definition).

The DFB pump laser diode is mounted on a piezo translation stage to adjust the injection phase[34], an actuator that can readily be achieved through on-chip heaters[41]. To reduce the device footprint and allow for more resonators on the chip, we have omitted this feature. The transmitted light is collected by an optical fibre whose tip is immersed in index-matching gel to suppress parasitic reflection. An overview of the setup is shown in Fig. 3a. The laser's emission wavelength can be tuned via its drive current. As long as the laser diode does not receive a resonant injection from the microresonator, it is free running. When it is close in frequency to the microresonator resonance, a strong resonant backwards wave is generated, providing frequency-selective optical feedback resulting in SIL.

We slowly (within approximately 10 s) tune the DFB's electrical drive current to scan the emission wavelength across the pump resonance, towards longer wavelength. During the laser scan, we monitor the transmitted power as well as the power of a filtered spectral portion of the long-wavelength wing of the generated microcombs (as an indicator for comb formation). Both are shown along with the DFB diode's drive current in Fig. 3b. Here, the SIL regime is clearly evidenced by a sharp drop in the transmission that, after optimizing the injection phase, extends over a wide range of electrical drive current values. The DKS regime is marked by the non-zero filtered transmitted power.
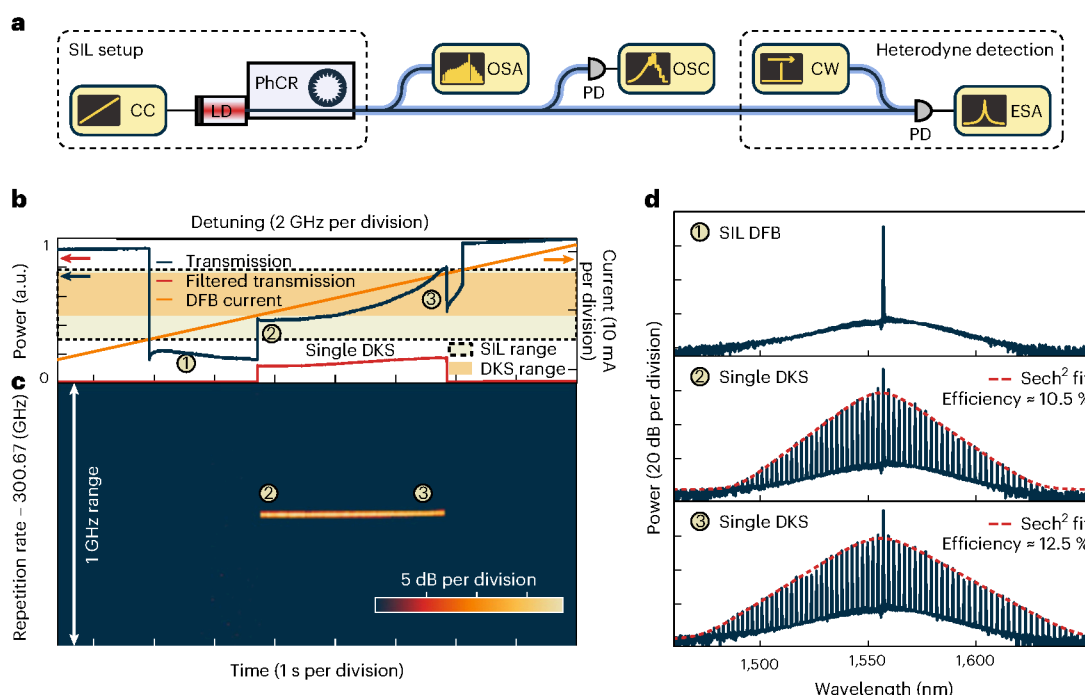
free spectral range (FSR), corresponding to a modulated waveform with a single intensity maximum. Such behaviour has been observed in PhCRs driven by an external continuous-wave laser[44]. Here, assuming symmetric power in the forwards and backwards pump mode, we estimate analytically the condition for exclusive single-DKS formation (see equation (29) in Supplementary Information) as

$$\frac{\gamma}{\kappa} > \frac{f^2}{8}. \tag{2}$$

Note that, owing to the small power asymmetry between forwards and backwards modes, the actual required value will be slightly higher.

The presented criteria enable us to tailor the synthetic back-reflection and to demonstrate a self-injection-locked soliton source, operating deterministically and exclusively in the single-DKS regime by design.

In preparation for the experiments, a range of photonic chip-integrated silicon nitride PhCRs (embedded in silica cladding) with varying corrugation amplitude (approximately 10–50 nm) were fabricated in a commercial foundry process (Ligentec) based on ultraviolet (UV) stepper lithography, compatible with wafer-level production. The resonators' FSR was 300 GHz (radius 75 µm), and their waveguide's height and mean width (800 and 1,600 nm, respectively) were chosen

Fig. 3 | Synthetic reflection-enabled DKS generation. a, The experimental setup. CC, current controller; LD, laser diode; OSA and ESA, optical and electrical spectrum analysers, respectively; OSC, oscilloscope; CW, continuous-wave laser; PD, photodiode. **b**, The total transmission (blue) and the bandpass-filtered microcomb power (see the main text) (red; filter offset from the pump, indicates comb formation) measured during a laser scan towards longer wavelengths. The orange line corresponds to the driving current. SIL and (single) DKS ranges on the current axis are highlighted. The horizontal axis indicates the free-running laser detuning and the experiment time. **c**, The repetition rate signal recorded during the same laser scan as in **b**, measured via heterodyne detection (see the main text). **d**, Optical spectra measured within the SIL range for CW SIL ① and SIL-based single-DKS states ② and ③, at different detunings as indicated by the corresponding circled numbers in **b**.

To confirm DKS generation, we record the 300 GHz DKS repetition rate beat note and the optical spectrum. As the repetition rate signal is not directly detectable, modulation side-bands around a pair of adjacent DKS comb lines are generated electro-optically. Their heterodyne beating with the DKS comb lines creates a signal at lower frequency, from which the repetition rate can be reconstructed[57]. Figure 3c shows the reconstructed repetition rate signal obtained during the DFB laser scan, and Fig. 3d shows optical spectra that correspond to different current values.

Upon entering the SIL regime, we observe at first only the single optical frequency of the SIL pump laser (Fig. 3d, ①). Continuing the scan, we next observe an abrupt transition into a single-DKS microcomb state (Fig. 3d, ②). Such single-DKS states are characterized by a smooth squared hyperbolic secant amplitude and a pulse repetition rate that corresponds to the resonator's FSR. These properties are highly desirable for applications. As the scan proceeds, the spectrum becomes broader (Fig. 3d, ③), which is an experimental manifestation of access to a range of detunings. This is also manifested in the slope of the transmission signal in the DKS state. Scanning even further causes the DKS to disappear and the system to return to CW SIL operation (with a spectrum similar to that in Fig. 3d, ①), before eventually exiting the SIL regime entirely. When repeated, each scan shows the same SIL dynamics, including deterministic single-DKS generation, independent of the scan speed (Supplementary Fig. 5). Turing patterns, noisy comb states and multi-DKS regimes are absent, in contrast to previously demonstrated self-injection-locked DKS. A detailed comparison between samples with different levels of backscattering $2\gamma/\kappa$ is provided in Supplementary Fig. 2, showing noisy or multi-DKS states as well as a drastically reduced extend of the single-DKS range for low values of $2\gamma/\kappa$.

Although not pursued here, we note that the pump to DKS conversion efficiency in states ② and ③ is 10.5% and 12.5%, respectively, considerably higher than what would be expected in conventional resonators. This is a consequence of the mode splitting, shifting the pumped resonance effectively closer to the pump laser, as explored previously in coupled ring resonators[50]. We also confirm that synthetic reflection does not lead to higher noise in an injection-locked regime, neither for continuous-wave lasing nor for a DKS, as further detailed in Supplementary Fig. 4). To demonstrate the deterministic and exclusive single-DKS generation, we repeatedly turn the diode's current on and off by using an automated procedure. We monitor the comb power (filtered transmission) (Fig. 4a) and record the optical spectrum created in each on–off cycle (Fig. 4b). Each time, a single DKS is generated.

Conclusion

We demonstrate self-injection-locked soliton microcombs based on synthetic reflection that operate exclusively and deterministically in the desirable single-DKS regime. These characteristics are achieved predictably and by design via suitably tailoring the synthetic reflection, in marked contrast to conventional self-injection locking that relies on random imperfection-based scattering. Importantly, synthetic reflection can ensure robust overlap between the DKS and self-injection locking ranges and, owing to its fast dynamics, mitigate thermal effects that could otherwise prevent access to DKS states. Considering bi-directional propagation in the resonator, we derive analytic design criteria that permit transfer of the presented results to alternative resonator geometries and material platforms. Predictable system characteristics, in conjunction with the scalable, widely accessible fabrication process, the low-cost components and the ease of operation without fast actuators, meet
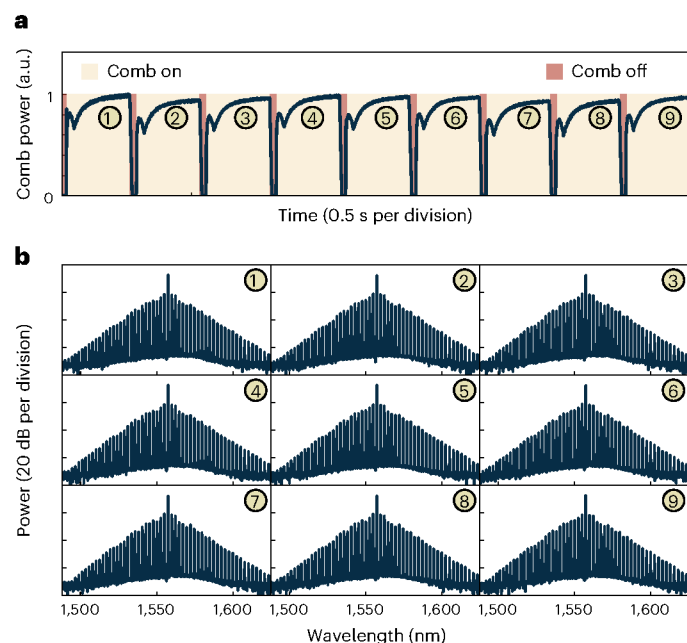
Fig. 4 | Deterministic on–off switching of single DKS. a, The bandpass-filtered power (where the filter is offset from the pump) measured during nine consecutive on–off switching cycles. In each cycle, the laser diode current is abruptly turned off and then ramped back up to the preset value. **b**, Optical spectra recorded in the respective on-phase of each cycle.

important requirements for scaling microcomb technology into large-volume applications.

Further research may explore extending the presented results to combs in the backwards direction (Supplementary Section 5), effectively blue-detuned DKS combs with potentially even higher conversion efficiency[50] or multiple pump wavelengths[58]. In addition, the novel concept of synthetic reflection may be translated to other integrated photonic systems, including normal dispersion combs[59,60], optical parametric oscillators[46], integrated tunable lasers[61,62] and novel quantum light sources[63,64].

Online content

Any methods, additional references, Nature Portfolio reporting summaries, source data, extended data, supplementary information, acknowledgements, peer review information; details of author contributions and competing interests; and statements of data and code availability are available at https://doi.org/10.1038/s41566-023-01367-x.

References

1. Vahala, K. J. Optical microcavities. *Nature* **424**, 839–846 (2003).
2. Del'Haye, P. et al. Optical frequency comb generation from a monolithic microresonator. *Nature* **450**, 1214–1217 (2007).
3. Sayson, N. L. B. et al. Octave-spanning tunable parametric oscillation in crystalline Kerr microresonators. *Nat. Photon.* **13**, 701–706 (2019).
4. Herr, T. et al. Temporal solitons in optical microresonators. *Nat. Photon.* **8**, 145–152 (2014).
5. Kippenberg, T. J., Gaeta, A. L., Lipson, M. & Gorodetsky, M. L. Dissipative Kerr solitons in optical microresonators. *Science* **361**, eaan8083 (2018).
6. Diddams, S. A., Vahala, K. & Udem, T. Optical frequency combs: coherently uniting the electromagnetic spectrum. *Science* **369**, eaay3676 (2020).
7. Leo, François et al. Temporal cavity solitons in one-dimensional Kerr media as bits in an all-optical buffer. *Nat. Photon.* **4**, 471–476 (2010).
8. Brasch, V. et al. Photonic chip-based optical frequency comb using soliton Cherenkov radiation. *Science* **351**, 357–360 (2016).
9. Gaeta, A. L., Lipson, M. & Kippenberg, T. J. Photonic-chip-based frequency combs. *Nat. Photon.* **13**, 158–169 (2019).
10. Marin-Palomo, P. et al. Microresonator-based solitons for massively parallel coherent optical communications. *Nature* **546**, 274–279 (2017).
11. Jørgensen, A. A. et al. Petabit-per-second data transmission using a chip-scale microcomb ring resonator source. *Nat. Photon.* **16**, 798–802 (2022).
12. Trocha, P. et al. Ultrafast optical ranging using microresonator soliton frequency combs. *Science* **359**, 887–891 (2018).
13. Suh, M.-G. & Vahala, K. J. Soliton microcomb range measurement. *Science* **359**, 884–887 (2018).
14. Suh, M.-G. et al. Searching for exoplanets using a microresonator astrocomb. *Nat. Photon.* **13**, 25–30 (2019).
15. Obrzud, E. et al. A microphotonic astrocomb. *Nat. Photon.* **13**, 31–35 (2019).
16. Suh, M.-G., Yang, Q.-F., Yang, K. Y., Yi, X. & Vahala, K. J. Microresonator soliton dual-comb spectroscopy. *Science* **354**, 600–603 (2016).
17. Liang, W. et al. High spectral purity Kerr frequency comb radio frequency photonic oscillator. *Nat. Commun.* **6**, 7957 (2015).
18. Lucas, E. et al. Ultralow-noise photonic microwave synthesis using a soliton microcomb-based transfer oscillator. *Nat. Commun.* **11**, 374 (2020).
19. Feldmann, J. et al. Parallel convolutional processing using an integrated photonic tensor core. *Nature* **589**, 52–58 (2021).
20. Xu, X. et al. 11 TOPS photonic convolutional accelerator for optical neural networks. *Nature* **589**, 44–51 (2021).
21. Bai, B. et al. Microcomb-based integrated photonic processing unit. *Nat. Commun.* **14**, 66 (2023).
22. Guo, H. et al. Universal dynamics and deterministic switching of dissipative Kerr solitons in optical microresonators. *Nat. Phys.* **13**, 94–102 (2017).
23. Bao, C. et al. Spatial mode-interaction induced single soliton generation in microresonators. *Optica* **4**, 1011–1015 (2017).
24. Obrzud, E., Lecomte, S. & Herr, T. Temporal solitons in microresonators driven by optical pulses. *Nat. Photon.* **11**, 600–607 (2017).
25. Rowley, M. et al. Self-emergence of robust solitons in a microcavity. *Nature* **608**, 303–309 (2022).
26. Zhang, S. et al. Sub-milliwatt-level microresonator solitons with extended access range using an auxiliary laser. *Optica* **6**, 206–212 (2019).
27. Li, Q. et al. Stably accessing octave-spanning microresonator frequency combs in the soliton regime. *Optica* **4**, 193–203 (2017).
28. Weng, H. et al. Dual-mode microresonators as straightforward access to octave-spanning dissipative Kerr solitons. *APL Photon.* **7**, 066103 (2022).
29. Wildi, T., Brasch, V., Liu, J., Kippenberg, T. J. & Herr, T. Thermally stable access to microresonator solitons via slow pump modulation. *Opt. Lett.* **44**, 4447–4450 (2019).
30. He, Y. et al. Self-starting bi-chromatic LiNbO₃ soliton microcomb. *Optica* **6**, 1138–1144 (2019).
31. Bai, Y. et al. Brillouin–Kerr soliton frequency combs in an optical microresonator. *Phys. Rev. Lett.* **126**, 063901 (2021).
32. Vasil'ev, V. V. et al. High-coherence diode laser with optical feedback via a microcavity with 'whispering gallery' modes. *Quantum Electron.* **26**, 657 (1996).
33. Liang, W. et al. Whispering-gallery-mode-resonator-based ultranarrow linewidth external-cavity semiconductor laser. *Opt. Lett.* **35**, 2822–2824 (2010).

34. Kondratiev, N. M. et al. Self-injection locking of a laser diode to a high-*Q* WGM microresonator. *Opt. Express* **25**, 28167 (2017).

35. Jin, W. et al. Hertz-linewidth semiconductor lasers using CMOS-ready ultra-high-*Q* microresonators. *Nat. Photon.* **15**, 346–353 (2021).

36. Pavlov, N. G. et al. Narrow-linewidth lasing and soliton Kerr microcombs with ordinary laser diodes. *Nat. Photon.* **12**, 694–698 (2018).

37. Stern, B., Ji, X., Okawachi, Y., Gaeta, A. L. & Lipson, M. Battery-operated integrated frequency comb generator. *Nature* **562**, 401–405 (2018).

38. Raja, A. S. et al. Electrically pumped photonic integrated soliton microcomb. *Nat. Commun.* **10**, 680 (2019).

39. Shen, B. et al. Integrated turnkey soliton microcombs. *Nature* **582**, 365–369 (2020).

40. Voloshin, A. S. et al. Dynamics of soliton self-injection locking in optical microresonators. *Nat. Commun.* **12**, 235 (2021).

41. Xiang, C. et al. Laser soliton microcombs heterogeneously integrated on silicon. *Science* **373**, 99–103 (2021).

42. Gorodetsky, M. L., Pryamikov, A. D. & Ilchenko, V. S. Rayleigh scattering in high-*Q* microspheres. *J. Opt. Soc. Am. B* **17**, 1051–1057 (2000).

43. Arbabi, A., Kang, Y. M., Lu, C.-Y., Chow, E. & Goddard, L. L. Realization of a narrowband single wavelength microring mirror. *Appl. Phys. Lett.* **99**, 091105 (2011).

44. Yu, S.-P. et al. Spontaneous pulse formation in edgeless photonic crystal resonators. *Nat. Photon.* **15**, 461–467 (2021).

45. Lu, X., McClung, A. & Srinivasan, K. High-*Q* slow light and its localization in a photonic crystal microring. *Nat. Photon.* **16**, 66–71 (2022).

46. Black, J. A. et al. Optical-parametric oscillation in photonic-crystal ring resonators. *Optica* **9**, 1183–1189 (2022).

47. Yang, K. Y. et al. Multi-dimensional data transmission using inverse-designed silicon photonics and microcombs. *Nat. Commun.* **13**, 7862 (2022).

48. Lucas, E., Yu, S.-P., Briles, T. C., Carlson, D. R. & Papp, S. B. Tailoring microcombs with inverse-designed, meta-dispersion microresonators. *Nat. Photon.* **17**, 943–950 (2023).

49. Herr, T. et al. Universal formation dynamics and noise of Kerr-frequency combs in microresonators. *Nat. Photon.* **6**, 480–487 (2012).

50. Helgason, Ó. B. et al. Surpassing the nonlinear conversion efficiency of soliton microcombs. *Nat. Photon.* **17**, 992–999 (2023).

51. Godey, C., Balakireva, I. V., Coillet, A. & Chembo, Y. K. Stability analysis of the spatiotemporal Lugiato-Lefever model for Kerr optical frequency combs in the anomalous and normal dispersion regimes. *Phys. Rev. A* **89**, 063814 (2014).

52. Kondratiev, N. M. & Lobanov, V. E. Modulational instability and frequency combs in whispering-gallery-mode microresonators with backscattering. *Phys. Rev. A* **101**, 013816 (2020).

53. Tan, T. et al. Gain-assisted chiral soliton microcombs. Preprint at https://arxiv.org/abs/2008.12510 (2020).

54. Barashenkov, I. V. & Smirnov, Y. S. Existence and stability chart for the ac-driven, damped nonlinear Schrödinger solitons. *Phys. Rev. E* **54**, 5707–5725 (1996).

55. Balakireva, I. V. & Chembo, Y. K. A taxonomy of optical dissipative structures in whispering-gallery mode resonators with Kerr nonlinearity. *Philos. Trans. R. Soc. A* **376**, 20170381 (2018).

56. Del'Haye, P., Arcizet, O., Gorodetsky, M. L., Holzwarth, R. & Kippenberg, T. J. Frequency comb assisted diode laser spectroscopy for measurement of microcavity dispersion. *Nat. Photon.* **3**, 529–533 (2009).

57. Del'Haye, P., Papp, S. B. & Diddams, S. A. Hybrid electro-optically modulated microcombs. *Phys. Rev. Lett.* **109**, 263901 (2012).

58. Chermoshentsev, D. A. et al. Dual-laser self-injection locking to an integrated microresonator. *Opt. Express* **30**, 17094 (2022).

59. Xue, X., Qi, M. & Weiner, A. M. Normal-dispersion microresonator kerr frequency combs. *Nanophotonics* **5**, 244–262 (2016).

60. Lihachev, G. et al. Platicon microcomb generation using laser self-injection locking. *Nat. Commun.* **13**, 1771 (2022).

61. Corato-Zanarella, M. et al. Widely tunable and narrow-linewidth chip-scale lasers from near-ultraviolet to near-infrared wavelengths. *Nat. Photon.* **17**, 157–164 (2023).

62. Lihachev, G. et al. Frequency agile photonic integrated external cavity laser. Preprint at https://arxiv.org/abs/2303.00425 (2023).

63. Zhao, Y. et al. Near-degenerate quadrature-squeezed vacuum generation on a silicon-nitride chip. *Phys. Rev. Lett.* **124**, 193601 (2020).

64. Lu, H.-H. et al. Bayesian tomography of high-dimensional on-chip biphoton frequency combs with randomized measurements. *Nat. Commun.* **13**, 4338 (2022).

Publisher's note Springer Nature remains neutral with regard to jurisdictional claims in published maps and institutional affiliations.

Methods

Numerical model

To simulate the non-linear DKS and breathing DKS existence range in Fig. 1c, we consider a system of coupled mode equations[65,66] for forward a_μ and backward b_μ mode amplitudes, where μ denotes the relative (longitudinal) mode number with respect to the pump mode ($m_0 \leftrightarrow \mu = 0$):

$$\partial_t a_\mu = -(1 + i\zeta_\mu) a_\mu + i \sum_{\mu' = \nu + \eta - \mu} a_\nu a_\eta a_{\mu'}^* + 2ia_\mu \sum_\eta |b_\eta|^2$$
$$+ i\delta_{\mu 0} \frac{2\gamma}{\kappa} b_\mu + f\delta_{\mu 0}$$
$$\partial_t b_\mu = -(1 + i\zeta_\mu) b_\mu + i \sum_{\mu' = \nu + \eta - \mu} b_\nu b_\eta b_{\mu'}^* + 2ib_\mu \sum_\eta |a_\eta|^2$$
$$+ i\delta_{\mu 0} \frac{2\gamma}{\kappa} a_\mu,$$

where $\zeta_\mu = \frac{2}{\kappa}(\omega_\mu - \omega_p - \mu D_1)$ is a dimensionless detuning defined by the pump laser frequency ω_p and the resonance frequencies $\omega_\mu = \omega_0 + D_1 \mu + \frac{1}{2} D_2 \mu^2$ (where $D_1/2\pi$ and $D_2/2\pi$ correspond to the FSR and the group velocity dispersion, and ω_0 is the resonance frequency of the pumped mode). $f = \sqrt{8\eta\omega_0 c n_2 P/(\kappa^2 n^2 V_{\text{eff}})}$ is the normalized pump power, with the coupling coefficient $\eta = 1/2$ (critical coupling), c is the speed of light, P is the pump power, n is the refractive index, n_2 is the non-linear refractive index and V_{eff} is the effective mode volume. Note that f_{th} in equation (1) is normalized in the same way as f. The third term in each equation corresponds to the cross-phase modulation by the respective counter-propagating waves, while the fourth term represents the coupling between forwards- and backwards-propagating waves. Instead of modelling the SIL dynamics by including laser rate equations, we numerically define the detuning. This approach cannot describe the abrupt transition from the free-running laser to the SIL state, but it remains valid for the specified detuning and can qualitatively capture the features observed in the experiment. Simulation parameters similar to those of the experimental system are used. The numerical simulation also enables us to compute the non-linear dispersion as illustrated in Supplementary Fig. 1.

Data availability

The code and data used to produce the plots can be found at https://zenodo.org/records/10118988.

Code availability

The numerical simulation code for the bi-directional non-linear coupled mode equation can be found at https://zenodo.org/records/10118988.

References

65. Chembo, Y. K. & Yu, N. Modal expansion approach to optical-frequency-comb generation with monolithic whispering-gallery-mode resonators. *Phys. Rev. A* **82**, 033801 (2010).
66. Hansson, T., Modotto, D. & Wabnitz, S. On the numerical simulation of Kerr frequency combs using coupled mode equations. *Opt. Commun.* **312**, 134–136 (2014).

Author contributions

A.E.U. and N.G.P. performed the experiments, T.W. designed the resonator and contributed to the experiments, J.D.J. and M.K. contributed to the experiments, A.E.U. analysed the data and T.H. supervised the work. A.E.U., T.W. and T.H. wrote the manuscript with input from all authors.

Competing interests

We declare that none of the authors have competing interests but disclose for transparency that J.D.J. and M.K. are cofounders of Enlightra and T.H., A.E.U., T.W. and M.K. are inventors on a patent application that may in aspects be related but is not limited to the subject matter disclosed in the manuscript.

Additional information

Supplementary information The online version contains supplementary material available at https://doi.org/10.1038/s41566-023-01367-x.

Correspondence and requests for materials should be addressed to Tobias Herr.

Peer review information *Nature Photonics* thanks Chee Wei Wong and the other, anonymous, reviewer(s) for their contribution to the peer review of this work.

Reprints and permissions information is available at www.nature.com/reprints.